HAL
open science

Radiatively limited dephasing and exciton dynamics in MoSe2 monolayers revealed with four-wave mixing microscopy

Tomasz Jakubczyk, Valentin Delmonte, Maciej Koperski, Karol Nogajewski, Clément Faugeras, Wolfgang Langbein, Marek Potemski, Jacek Kasprzak

To cite this version:

Tomasz Jakubczyk, Valentin Delmonte, Maciej Koperski, Karol Nogajewski, Clément Faugeras, et al.. Radiatively limited dephasing and exciton dynamics in MoSe2 monolayers revealed with four-wave mixing microscopy. Nano Letters, 2016, 16 (9), pp.5333-5339. 10.1021/acs.nanolett.6b01060 . hal-01357636

HAL Id: hal-01357636

https://hal.science/hal-01357636v1

Submitted on 1 Sep 2016

HAL is a multi-disciplinary open access archive for the deposit and dissemination of scientific research documents, whether they are published or not. The documents may come from teaching and research institutions in France or abroad, or from public or private research centers.

L'archive ouverte pluridisciplinaire **HAL**, est destinée au dépôt et à la diffusion de documents scientifiques de niveau recherche, publiés ou non, émanant des établissements d'enseignement et de recherche français ou étrangers, des laboratoires publics ou privés.

Radiatively limited dephasing and exciton dynamics in $MoSe_2$ monolayers revealed with four-wave mixing microscopy

Tomasz Jakubczyk,[†,‡] Valentin Delmonte,[†,‡] Maciej Koperski,[¶,§] Karol Nogajewski,[¶] Clément Faugeras,[¶] Wolfgang Langbein,[‖] Marek Potemski,[¶] and Jacek Kasprzak[*,†,‡]

†*Université Grenoble Alpes, Institut Néel, F-38000 Grenoble, France*

‡*CNRS, Institut Néel, "Nanophysique et semiconducteurs" group, F-38000 Grenoble, France*

¶*Laboratoire National des Champs Magnétiques Intenses, CNRS-UGA-UPS-INSA-EMFL, 25 Av. des Martyrs, 38042 Grenoble, France*

§*Institute of Experimental Physics, Faculty of Physics, University of Warsaw, ul. Pasteura 5, 02-093 Warsaw, Poland*

‖*Cardiff University School of Physics and Astronomy, The Parade, Cardiff CF24 3AA, UK*

E-mail: jacek.kasprzak@neel.cnrs.fr

Abstract

By implementing four-wave mixing micro-spectroscopy we measure coherence and population dynamics of the exciton transitions in monolayers of $MoSe_2$. We reveal their dephasing times T_2 and radiative lifetime T_1 in a sub-picosecond (ps) range, approaching $T_2=2T_1$, and thus indicating radiatively limited dephasing at a temperature of 6 K. We elucidate the dephasing mechanisms by varying the temperature and by

probing various locations on the flake exhibiting a different local disorder. At nanosecond range, we observe the residual FWM produced by the incoherent excitons, which initially disperse towards the dark states, but then relax back to the optically active states within the light cone. By introducing polarization-resolved excitation, we infer inter-valley exciton dynamics, revealing an initial polarization degree of around 30%, constant during the initial sub-picosecond decay, followed by the depolarization on a picosecond timescale. The FWM hyperspectral imaging reveals the doped and undoped areas of the sample, allowing to investigate the neutral exciton, the charged one or both transitions at the same time. In the latter, we observe the exciton-trion beating in the coherence evolution indicating their coherent coupling.

Introduction The identification of atomically-thin solids [1] resulted in the development of the intriguing physics of graphene, followed by the emerging technological applications.[2,3] Also, it stimulated a rapid progress in fundamental studies of thin films extracted from other than graphite layered materials, such as, semiconducting transition metal dichalcogenides (S-TMDs). The bandgap of S-TMDs, converts from indirect to direct, when reducing the material thickness to a single monolayer,[4] enabling exceptionally strong excitonic transitions. Owing to the breakdown of out of plane translational symmetry for two dimensional systems, the coupling of excitons with light is boosted,[5] resulting in their short radiative lifetime and thus increased oscillator strength μ. Excitons in S-TMD monolayers display large binding energies E_B of several hundreds of meV [6–9] - an increase by one to two orders of magnitude with respect to a typical semiconductor quantum well.[10,11] The observed excitonic absorption in S-TMDs reaches the values as high as 10 %,[12] illustrating an exceptionally strong μ in these systems and implying a radiative lifetime in the sub-picosecond (sub-ps) range,[13] as recently observed in monolayers of WSe_2 [14,15] and other emerging two-dimensional systems, namely nano-platelets.[27] The robust coupling with light is attractive in prospective applications, especially for photodetectors.[3] It is also appealing in optical fundamental studies, for instance in polaritonics [16] and nonlinear spectroscopy.[15,17,19]

The large μ in S-TMDs gives rise to a giant nonlinear optical response, which is investigated in this work via three-pulse four-wave mixing (FWM) micro-spectroscopy. This approach offers a direct access to the exciton coherence and population dynamics with a time resolution limited only by the duration of the laser pulses, which resonantly excite targeted optical transitions. Indeed, time-resolved non-resonant photoluminescence measurements ,[18] offer insufficient time-resolution to infer sub-ps evolution and involve complex relaxation pathways. Instead, resonant experiments ,[15,19] also investigating internal transitions [14] occurring in the THz domain, have recently revealed ultrafast radiative recombination of the exciton ground state in WSe_2.

In this work, we show that the optical dephasing time T_2 of the neutral exciton transition (EX) in a monolayer of $MoSe_2$ is intrinsically limited by the EX ultrafast radiative recombination T_1. In contrast to previous works inferring optical coherence in S-TMDs ,[15,19] we take advantage of the micro-spectroscopy approach, employing the laser beams focused down to the diffraction limited size of $0.7\,\mu$m (full width at half-maximum, FWHM). Such implementation is used to perform the FWM hyperspectral imaging ,[20] which discriminates the exciton charge state across the sample and helps to reveal the striking features of coherent coupling between the neutral and charged excitons. We demonstrate that the EX linear response inferred via micro-reflectance, is affected by the inhomogeneous broadening ξ also on a sub-μm scale, evidenced by the photon echo formation in the FWM transients .[21] The analysis of the FWM delay dependence yields $T_2 \simeq 2T_1$, occurring on a sub-picosecond timescale. A spatially-resolved study shows that T_2 depends on the local disorder varying on a sub-micron scale. From the temperature dependent homogenous linewidth we determine the dephasing due to phonon interaction. We also monitor the density dynamics of excitons, which is governed by the interplay between bright states within the light cone and various available dark states.

Sample & experiment The investigated $MoSe_2$ monolayer was fabricated by means of polydimethylsiloxane-based exfoliation of bulk crystals, purchased from HQ Graphene, and transferred onto a Si/SiO_2 substrate. Relatively large monolayer flakes of up to $(50 \times 50)\,\mu m^2$ size have been obtained and placed in an optical He-flow cryostat.

To infer both the coherence and the population dynamics of excitons, we retrieved their FWM by implementing a three-beam configuration [20] of the heterodyne spectral interferometry.[21] This technique has been proven as an efficient detection scheme of optical nonlinearities in a solid, until now only employed to retrieve wave mixing signals generated by individual transitions in semiconductor quantum dots.[20,21,25] FWM is an optical polarization created with short, resonant driving pulses; $\mathcal{E}_1$, $\mathcal{E}_2$ and $\mathcal{E}_3$, as depicted in Fig. 1 a. In the third-order ($\chi^{(3)}$) regime its amplitude is proportional to $\mu^4 \mathcal{E}_1^* \mathcal{E}_2 \mathcal{E}_3$. Thus, owing to a large μ, a dramatic enhancement of FWM is expected in $MoSe_2$ monolayers. Note that the * stands for the complex conjugate, which is the origin of the FWM rephasing in inhomogeneously broadened systems,[21] generating the photon echo (as also sketched in Fig. 1 a), which acts as a probe of the microscopic dephasing.

Micro-FWM spectroscopy requires the co-linear arrangement of the driving fields $\mathcal{E}_{1,2,3}$, which is enabled by phase-selecting the signal through optical heterodyning.[21] By employing acousto-optic modulation, $\mathcal{E}_{1,2,3}$ are frequency up-shifted by radio-frequencies, introducing controlled phase-drifts in their respective pulse trains generated by a Ti:Sapphire femtosecond laser. After acquiring the delays τ_{12} and τ_{23}, introduced by a pair of mechanical delay lines, $\mathcal{E}_{1,2,3}$ are recombined into a common spatial mode and are focused on the sample with the microscope objective. The reference beam $\mathcal{E}_r$, used in the heterodyne mixing and interferometric detection, is also focused at the sample, yet is vertically displaced with respect to $\mathcal{E}_{1,2,3}$ by around $12\mu m$.

The time-ordering of the pulses is presented on Fig. 1 a: measuring time-integrated FWM detected at the $\Omega_3 + \Omega_2 - \Omega_1$ heterodyne frequency, as a function of τ_{12} (τ_{23}), yields the coherence (population) dynamics of an optical transition. The FWM signal is measured in

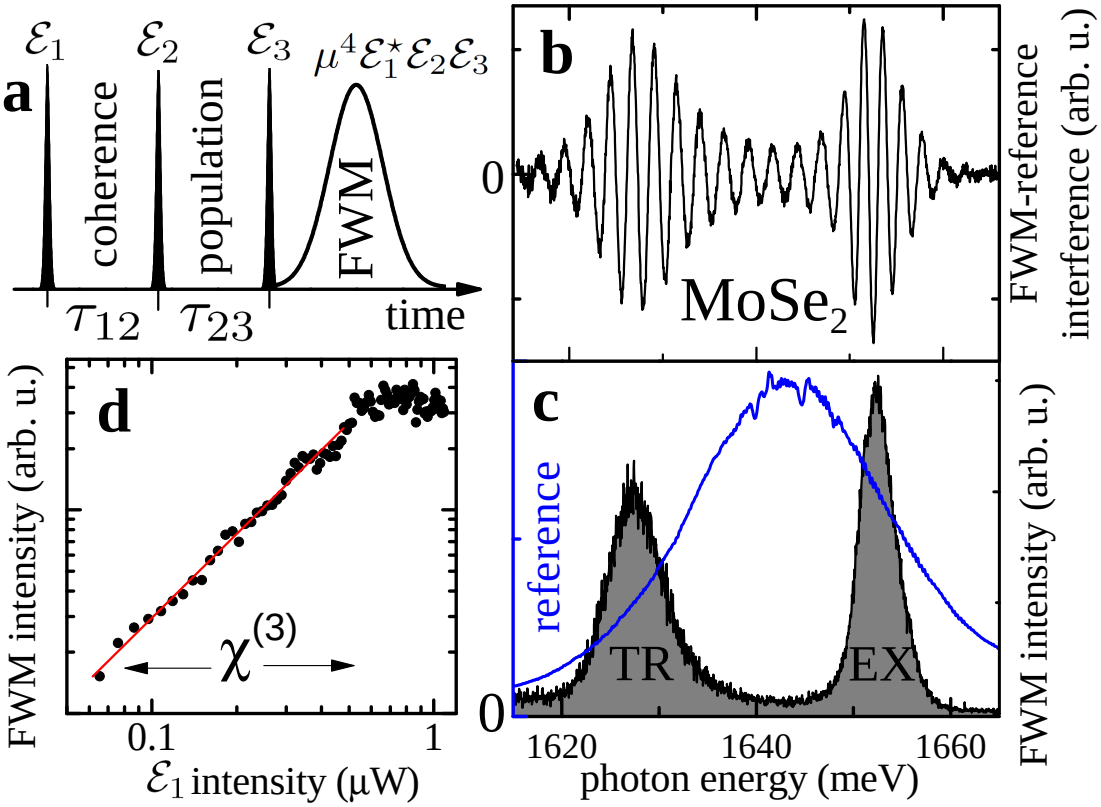

Figure 1: **Four-wave mixing spectroscopy of the $MoSe_2$ monolayer.** a) Pulse sequence employed in FWM experiments and related observables. b) FWM spectral interferogram obtained on the flake position displaying the exciton (EX) and trion (TR) transitions. c) FWM intensity (black) retrieved from b) via spectral interferometry. $\mathcal{E}_r$ is shown with a blue line. d) Spectrally integrated FWM intensity of EX as a function of $\mathcal{E}_1$ intensity, showing the driving range yielding the $\chi^{(3)}$ regime of the FWM.

reflectance, attaining a shot-noise detection limit and rejecting the resonant driving fields $\mathcal{E}_{1,2,3}$ with 10^6 (10^{12}) selectivity in field (intensity). The interference between the heterodyned signal and $\mathcal{E}_r$ is spectrally resolved with an imaging spectrometer. Further details regarding the current experimental implementation are given in Ref. [20].

In Fig. 1 b we present a typical spectral interference between $\mathcal{E}_r$ and the FWM at a temperature T=5 K for $\tau_{12} = 0$. The FWM intensity is retrieved by spectral interferometry and shown in Fig. 1 c. The signal consists of two transitions identified as the ground state-exciton (EX) and the single electron-trion transitions (TR).[22] In Fig. 1 d we present the FWM intensity of EX as a function of $\mathcal{E}_1$ intensity demonstrating a linear dependence in the

$\chi^{(3)}$ regime, as expected. Note that the FWM can be driven with a $\mathcal{E}_1$ intensity as low as a few tens of nW, corresponding to a few hundreds of photons per pulse $\mathcal{E}_1$ and generating a low carrier density, less than $10^9/\,\mathrm{cm}^2$. Such density is far below the saturation density [23] estimated at around $10^{13}/\,\mathrm{cm}^2$. In our study, we therefore consider the creation of excitons with K~ 0 center of mass momentum, which appear at the, K+ and K-, points of the Brillouin zone of the S-TMD crystal. Those excitons can either decay radiatively or disperse out of the light cone (K$> n\omega/c$) via phonon scattering. The latter process occupies dark exciton states, which relax back to K$< n\omega/c$ on a pico-second time scale and eventually recombine. Further relaxation pathways are scattering electrons and holes between the K-points.

Hyperspectral imaging An image of the studied $MoSe_2$ monolayer is shown in Fig. 2 and in the Table of Contents graphics. The micro-spectroscopy approach enables to perform FWM hyperspectral imaging ,[20,25] allowing to identify regions of the flake dominated by the FWM of EX or TR (see Fig. 2 b and c). Clearly, the two images are complementary, which permits to distinguish regions of different resident carrier concentration. In the following experiments, the performed imaging allowed us to selectively address EX or TR, or to drive simultaneously both transitions.

Performing micro-spectroscopy also permits to locally address sub-μm regions of smaller spectral inhomogeneous broadening with respect to the total area of the flake. To exemplify this, we have performed a statistical analysis of the micro-photoluminescence (PL) hyperspectral imaging. Similarly as in Fig. 1 c, confocally detected PL spectra yield EX and TR transitions, as displayed at the top of Fig. 2 d. We observe particularly bright emission, with a photon flux per second of $10^8 - 10^9$, indicating a high quantum yield.

For every spatial position, we have determined the integrated intensity for both transitions and their center energies. For the latter, we observe the spread over $\xi \simeq 10\,\mathrm{meV}$, as displayed at the bottom of Fig. 2 d. Interestingly, despite this large, macroscopic ξ, the trion binding energy Δ remains well defined, $\Delta = (28.8 \pm 0.3)\,\mathrm{meV}$. We note that the lower

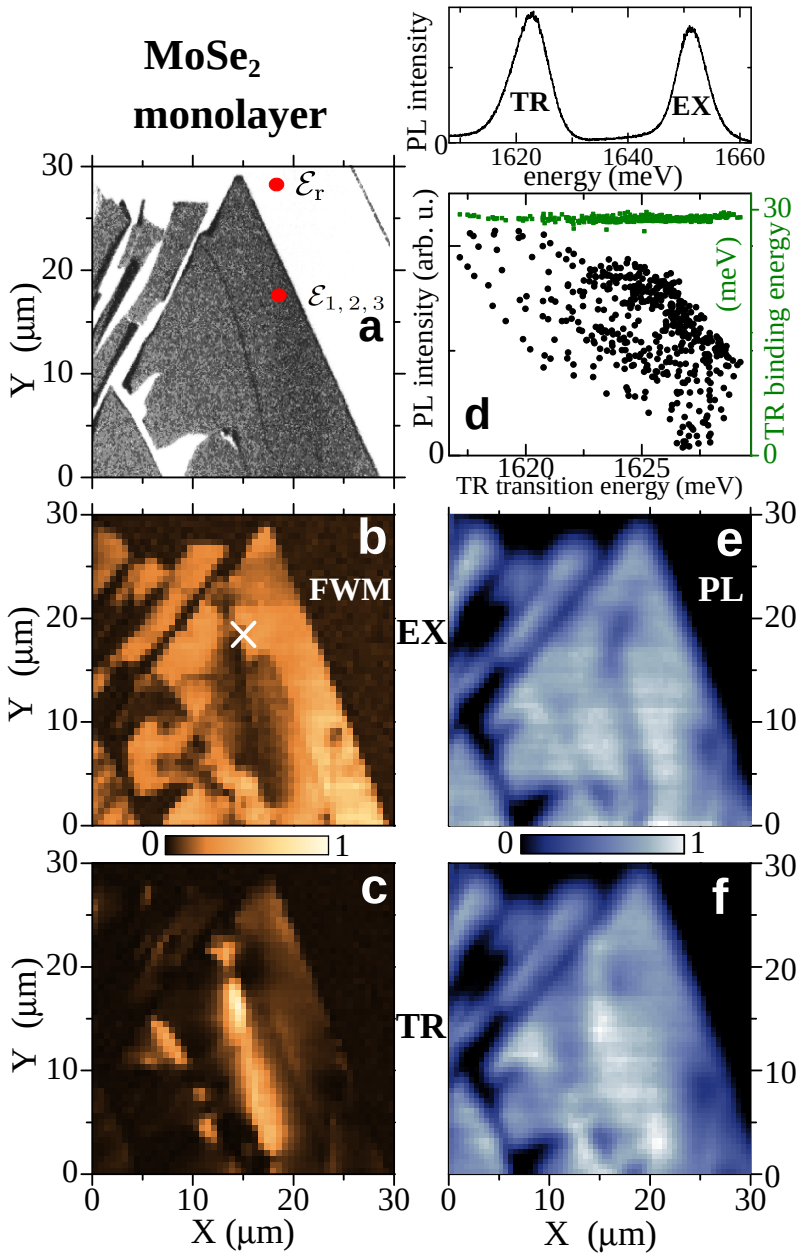

Figure 2: **Hyperspectral mapping of the $MoSe_2$ monolayer.** a) Optical contrast of the sample observed in reflectance. Red dots indicate $\mathcal{E}_{1,2,3}$ and $\mathcal{E}_r$. b)-c) Spatial imaging of the FWM amplitude, spectrally averaged over the exciton (b) response, centered at ~ 1650 meV and the trion (c) at ~ 1625 meV. Heterodyning at the FWM frequency $\Omega_3 + \Omega_2 - \Omega_1$ with $\tau_{12} = \tau_{23} = 50$ fs, T= 6 K. d) Top: A typical PL spectrum, non-resonantly excited at at $\sim$ 1750 meV ($\sim$ 710 nm) with $\simeq 0.1\,\mu$W average power arriving at the sample surface, displaying bright emission from EX and TR, with integrated count rate of 350kHz for each transition. Bottom: Correlation between the PL intensity of the TR (black) and its binding energy (green), as a function of its transition energy. e)-f) PL imaging of TR and EX, respectively. Excitation conditions as in d). Linear color scale, as shown by horizontal bars.

the TR transition energy, the higher its intensity is measured. This we believe reflects the distribution of residual electrons in the sample. Interestingly, however, such correlation is not observed for EX, i.e., the EX intensity is not sensitive to the apparent, in our sample changes in the charge density.

In Fig. 2 e and f we present the PL imaging spectrally integrated over EX and TR transition, respectively. By comparing it with Fig. 2 b and c, we point out two advantages of our original FWM imaging with respect to the routinely performed PL one. Firstly, owing to the third-power scaling of the FWM intensity with the excitation power, combined with heterodyning with $\mathcal{E}_{\mathrm{r}}$, the spatial resolution in the FWM imaging is enhanced [26] up to $0.3\lambda/\mathrm{NA} \approx 360\,\mathrm{nm}$, surmounting the standard diffraction limit by a factor of 2. Secondly, the FWM yields a significantly improved imaging selectivity of EX and TR across the flake. In fact, different properties are inferred in both experiments. The FWM directly probes μ of the resonantly generated excitons at the K-points of the valleys. Instead, the non-resonant PL reflects more complex carrier relaxation along the valleys towards their K-points, prior to the exciton formation, followed by their radiative recombination.

Coherence dynamics The strength of the FWM spectroscopy in assessing the coherence in solids lies in its capability to separate homogenous (γ) and inhomogeneous (ξ) contributions of the transition's spectral width. In particular, in a presence of ξ, the time-resolved FWM amplitude exhibits a photon echo,[15,27] which decays as $\exp\left(-2\tau_{12}/\mathrm{T}_2\right)$. Hence, to investigate the exciton coherence dynamics, we measured FWM as a function of τ_{12}. Time-resolved FWM amplitude of the EX transition, displayed in Fig. 3 a, clearly demonstrates formation of the photon echo. From its temporal width we estimate the local ξ to be in a few meV range. Fig. 3 b shows the time-integrated FWM as a function of τ_{12}. The data are modeled by a convolution of a Gaussian profile with an exponential decay. The former exhibits the FWHM width of 0.15 ps, reflecting duration of $\mathcal{E}_{1,2,3}$ impinging the sample. Instead, from the latter we retrieve at T=6 K the dephasing time $\mathrm{T}_2 = 2\hbar/\gamma = (620 \pm 20)\,\mathrm{fs}$,

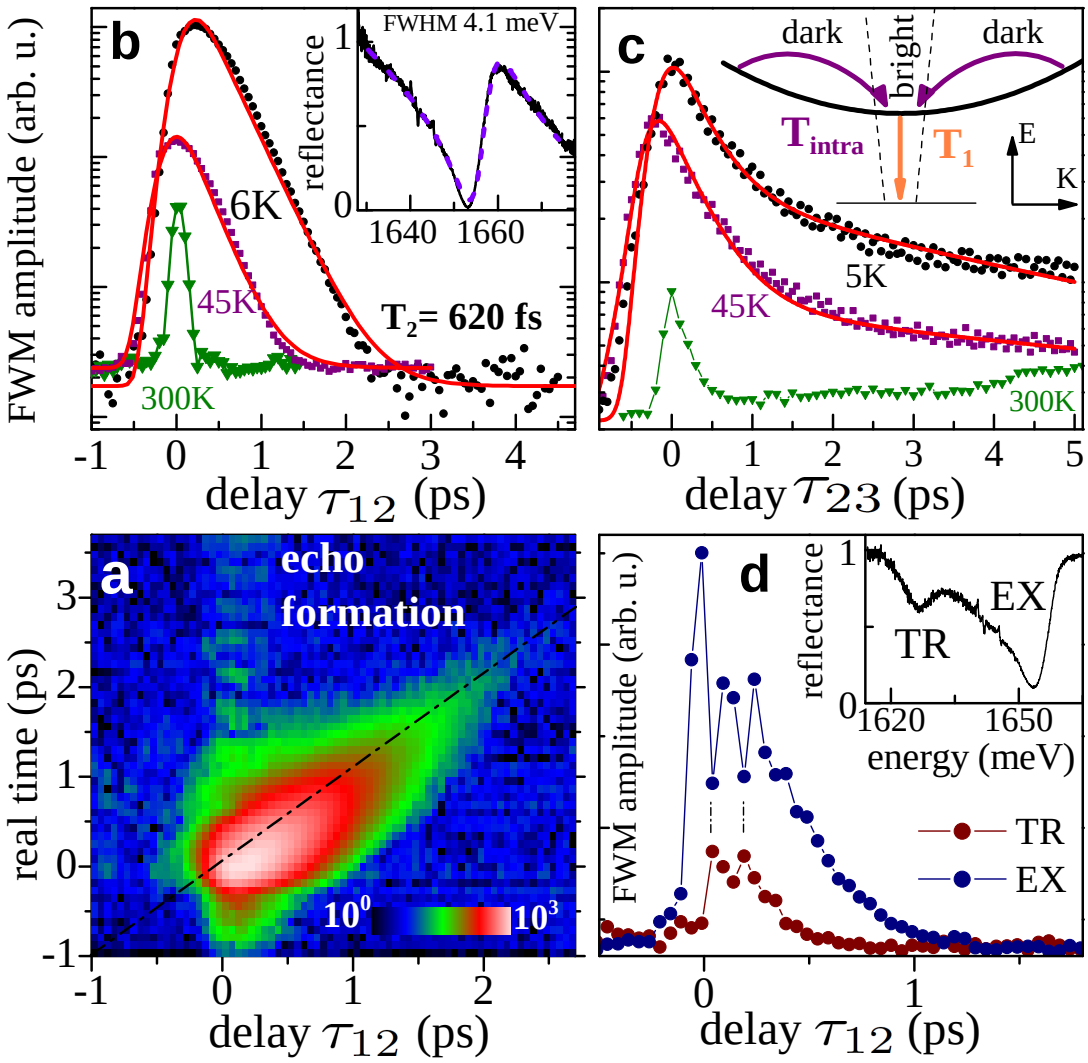

Figure 3: **Exciton dynamics in the $MoSe_2$ monolayer inferred with FWM microscopy**. a) Time-resolved FWM amplitude as a function of τ_{12}, showing formation of a photon echo: a Gaussian signal with a maximum for $t = \tau_{12}$. Logarithmic color scale given by the color bar. b) FWM amplitude as a function of τ_{12} retrieved from the EX at T= (6, 45, 300) K given by (black circles, purple squares and green triangles), respectively. The simulations yielding $T_2 \simeq (620, 520)$ fs are given by red traces. Inset: reflectance measured at T=6 K yielding 4.1 meV FWHM. c) Cartoon of the considered radiative recombination and intra-valley relaxation processes is presented in the inset. The initial dynamics of the EX population measured at $(5, 45, 300)$ K, color coding as in b). The results yield radiative lifetime T_1 and relaxation time T_{intra} (see main text). d) τ_{12} dependence of the FWM amplitude when simultaneously driving the EX (blue) and TR (brown) transitions, revealing a beating with 140 fs period, and thus indicating EX-TR coherent coupling. The location of the excitation is marked with a cross in Fig. 2 b, while the corresponding micro-reflectance spectrum is given in the inset.

and thus $\gamma \simeq 2.1\,\mathrm{meV}$ (FWHM). For simplicity, the dynamics owing to the echo formation process close to zero delay, has been here disregarded. The homogenous broadening γ is around twice smaller than the transition linewidth directly measured via micro-reflectivity, as shown in the inset of Fig. 3 b and also in FWM (see Fig. 1 c). We thus conclude that the line-shape remains affected by the inhomogeneous broadening ξ, even though a sub-μm area is probed.

With increasing temperature, T_2 is expected to decrease,[15] owing to phonon scattering. This is highlighted in Fig. 3 b. At T=45 K the dephasing accelerates and we measure $T_2 = (520 \pm 40)\,\mathrm{fs}$. At ambient temperature the dephasing occurs at a timescale faster than 100 fs and is not resolved by our setup, although a pronounced FWM is still measured. We note that for the TR transition at T=6 K we find $T_2 = (460 \pm 30)\,\mathrm{fs}$ and similar inhomogeneous broadening as for EX, also generating a photon echo as in Fig. 3 c (not shown). This shorter dephasing of the charged exciton, is tentatively interpreted in terms of the final state damping, due to the energy distribution of final state energies of the leftover electron.

In Fig. 3 c we present the coherence dynamics measured at the boundary of the doped and undoped regions of the flake, marked with a cross in Fig. 2 d, such that the FWM of both EX and TR is driven in tandem. We observe a beating, withstanding on both transitions during initial positive delays τ_{12}, up to around 700 fs when the TR coherence virtually vanishes. The beating period of $\zeta = 140\,\mathrm{fs}$ (marked with a pair of vertical lines), well corresponds to the EX - TR binding energy $\Delta = 2\pi\hbar/\zeta \simeq 29\,\mathrm{meV}$ and thus indicates their coherent coupling.[28,29]

To gain a deeper understanding of the exciton ultrafast dynamics, we have combined the enhanced spatial and temporal resolution of our experiment and we have performed spatially-resolved dephasing study at T=6 K. Within an area of 8 μm by 8 μm, displaying uniquely the EX transition, we have scanned the coherence dynamics with a spatial step of 0.66 μm. The analysis of the obtained statistics of dephasing, reveals variations of T_2

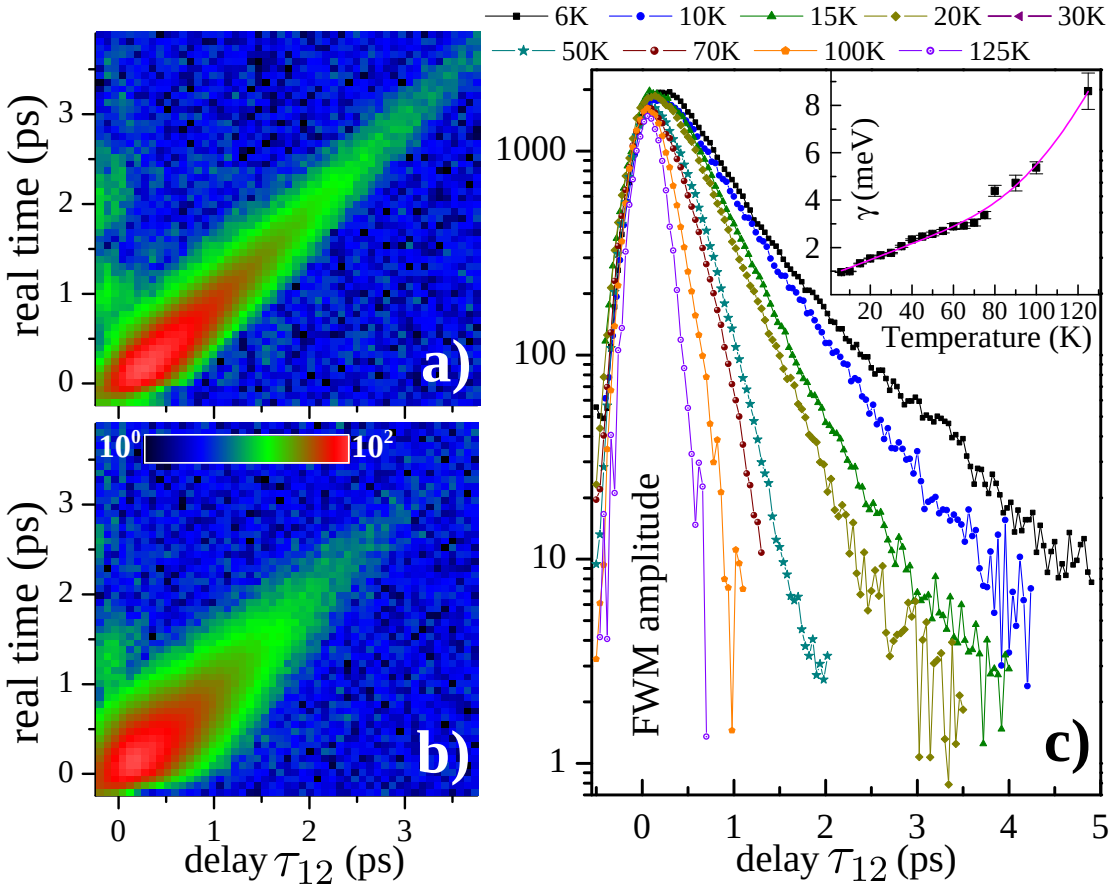

Figure 4: **Impact of a local disorder and temperature on the exciton dephasing in the $MoSe_2$ monolayer**. a) Time-resolved FWM amplitude, measured on the location displaying a larger ξ, showing a temporarily narrowed photon echo. The observed increased dephasing time with respect to Fig. 3 attributed to a localization induced increase of the radiative lifetime T_1. b) as a) but measured on the area showing a broader echo and thus smaller ξ. A weaker localization yields a shorter $T_1 = T_2/2$ than in a). Logarithmic color scale over two orders of magnitude. c) FWM amplitude dynamics as a function of temperature measured on the area as in a). Above T=125 K the dephasing is faster than the temporal resolution of the experiment. The temperature dependent homogenous broadening $\gamma = 2\hbar/T_2$ (inset) indicates the phonon-induced dephasing mechanism. For clarity, the fits are not shown.

within the probed area from around 0.5 ps up to 1.5 ps. Interestingly, the locations on the flake yielding the shortest T_2 also display the broadest photon echo, and thus the smallest ξ. Conversely, the longest T_2 is measured on the areas characterized by a larger ξ, and thus showing the narrowest photon echo, here limited by the temporal duration of the laser pulses. An example of such two representative cases is displayed in Fig. 4 a and b. The

spatially-resolved dephasing experiment indicates that T_2 is governed by a local disorder, realizing various localization potentials. The resulting spatially-dependent coherence volume of EX has a direct impact on its radiative lifetime T_1: the fastest recombination is expected at the areas of the smallest ξ, as indeed measured.

In Fig. 4 c we present the coherence dynamics on the chosen area exhibiting an increased T_2, measured from 6 K to 150 K. The data clearly show a gradual decrease of T_2 with temperature from 1.4 ps to 0.2 ps respectively, adding to the measurements shown in Fig. 3 b. The retrieved $\gamma = 2\hbar/T_2$ is plotted in the inset. It can be modeled with a linear dependence and an additional bosonic term :[41] $\gamma(T) = \gamma_0 + aT + b/(\exp(E_1/k_B T) - 1)$. The linear term ($\gamma_0 = (0.78 \pm 0.11)$ meV, $a = (0.03 \pm 0.003)$ meV/K) is due to low energy acoustic phonons. The latter term, with the energy ($E_1 = 43 \pm 4$)meV and $b = (187 \pm 75)$ meV, could be attributed to thermal activation of higher energy optical phonons .[41] The phonon dephasing mechanisms are therefore similar as in semiconductor quantum wells.

Population dynamics In the following, the FWM is employed to infer the EX population dynamics after their resonant and selective excitation in a given valley ($\mathcal{E}_1$ and $\mathcal{E}_2$, denoted as $\mathcal{E}_{1,2}$, are co-circularly polarized). They arrive at the flake with virtually no delay generating exciton population. Owing to the large μ, the excitons exhibit fast radiative decay. Nevertheless, they still experience scattering [24] for instance induced by defects, disorder and phonons, which can efficiently redistribute them out of the light cone (marked with dashed lines in the inset of Fig. 3 c), toward K$> n\omega/c$. This type of scattering is particularly efficient in S-TMDs: due to heavy masses (and thus flat bands at the bottom of the branches) and large γ, the excitons' center of mass scatter out of the light cone at practically no cost in energy. As a result, the major part of the created population instantly decays with its radiative lifetime T_1, while the remaining part spreads along the dispersion branch populating dark states (i.e. outside the light cone). Also a part of these excited excitons eventually relax toward the bottom of the valley with a characteristic time T_{intra} and recombine radia-

tively, as depicted in Fig. 3 c. In the dynamics probed with FWM, we disregard the influence of strongly localized, quantum-dot like states, due to their small density and we disregard non-radiative Auger processes ,[14] as we operate at low exciton densities.

The FWM therefore probes all the above mentioned processes via τ_{23} dependence. This is shown in Fig. 3 c, for the EX (obtained the same spatial position as in Fig. 3 b) for driving upon co-circular polarization of $\mathcal{E}_{1,2,3}$. The data are modeled with a double exponential decay convoluted with the Gaussian laser pulse, showing temporal width of 0.16 ps (FWHM). From the initial decay we retrieve the exciton lifetime of $T_1 = (390 \pm 20)$ fs, while the FWM for further delays τ_{23} yields the intra-valley relaxation time of $T_{intra} = (4.3 \pm 0.6)$ ps. At T=45 K we measure instead (T_1, T_{intra})=$(0.42 \pm 0.01, 6.84 \pm 0.38)$ ps. An increase of T_{intra} with temperature is attributed to Boltzmann distribution of excitons, allowing for reaching higher energies and K-vectors out of the light cone, and also to access different dark states offered by the structure of the valley-excitons.

A physical picture arising from the FWM experiment at low temperature is that the initial exciton decay with the time T_1, covering an order of magnitude in amplitude (see Fig. 3 c), is due to the radiative recombination, while the non-radiative processes are of minor impact. Importantly, comparing the T_1 with T_2 times, we conclude that the dephasing is principally due to the radiative decay, nearing to the radiative limit. Observation of the radiatively limited dephasing is a prerequisite for implementing more advanced optical coherent control schemes in S-TMDs.

We point out that the dynamics of the secondary, incoherent excitons - here probed by τ_{23} dependence of FWM - is particularly complex and might be influenced by a set of unconventional features present in S-TMDs. One should bear in mind coupling with and scattering toward counter-polarized K-valleys and spin-split bands, relevant in formation of exciton complexes. In fact, triple-degeneracy of the K-valleys, enables various configurations for bright and dark excitons states, as previously considered for other systems hosting multi-excitons .[30,31] We also point out exotic dispersion relations for the center-of-mass mo-

mentum.[32] Thus, we refrain from firm interpretation and first-principle modeling of the secondary exciton dynamics, displayed in Fig. 5 on a 100 ps time scale.

Inter-valley dynamics Below, we present the FWM results obtained upon polarization-resolved driving, employed to investigate exciton scattering between counter-polarized valleys, and thus testing the robustness of the pseudo-spin degree of freedom. The reciprocal space of TMDs monolayers displays nonequivalent bands with the extrema at K-points,[33–35] labeled as K_+ and K_-. The dipole-allowed transitions in these two valleys can be selectively addressed by circularly polarized light, σ^+ and σ^-, respectively. The light helicity is therefore considered as an asset to drive, manipulate and read the state of the valley subspaces. The valley polarization,[34] although protected by the strong spin-orbit splitting in the valence band, decays mainly due to the to electron-hole exchange interaction.[36,37] Since the stability of this degree of freedom is required in prospective applications of TMDs, intense efforts are currently devoted to study its dynamics and to reveal the mechanisms that govern it,[38] in particular in a presence of spin-forbidden transitions.[12,39,42–44]

To infer the exciton inter-valley dynamics, we implemented polarization-resolved excitation of the FWM signal. Specifically, $\mathcal{E}_3$ and $\mathcal{E}_\mathrm{r}$ are set as co-circular. Instead, the circular polarization of $\mathcal{E}_{1,2}$ is opposite, such that FWM probes the conversion of the exciton population between K+ and K- valleys,[35] as depicted in Fig. 5. Instead, to probe the exciton dynamics in the same valley, we set the co-circular polarization of $\mathcal{E}_{1,2}$ and $\mathcal{E}_3$. The measurement is presented in Fig. 5 (bottom). As in Fig. 3 c, we observe an initial fast decay of the radiatively recombining excitons within the first ps and subsequent recombination of the secondary excitons. The early dynamics for both polarization configuration is not the same during initial several ps of τ_{23}. Instead, for longer delays, $\tau_{23} > 10$ ps, the measured FWM (generated by the secondary excitons) is the same for both driving configurations.

We calculate the FWM circular polarization degree, which we define as $\rho(\tau_{23}) = \frac{R(\tau_{23},\sigma+)-R(\tau_{23},\sigma-)}{R(\tau_{23},\sigma+)+R(\tau_{23},\sigma-)} \times 100\%$, where R denotes the spectral FWM amplitude. The resulting $\rho(\tau_{23})$ is plotted at the

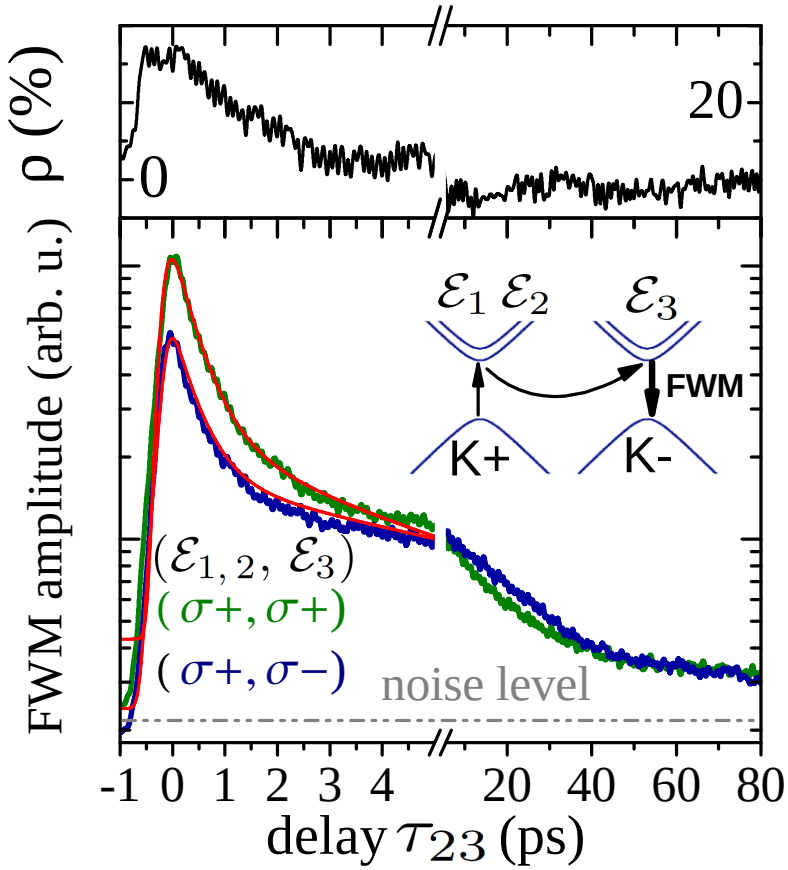

Figure 5: **Inter-valley population dynamics in the $MoSe_2$ monolayers investigated with the polarization-resolved driving of the FWM**. Bottom: FWM amplitude versus τ_{23} of the EX transition obtained at T=6 K upon co- (green circles) and cross-circular (blue squares) setting of $(\mathcal{E}_{1,2}, \mathcal{E}_3)$. The modeling, as in Fig. 3 c, is displayed as red lines. Equivalent dynamics have been measured (not shown) for a counter-polarized driving ($\sigma+ \mapsto \sigma-$). Inset: Rationale of the inter-valley dynamics probed with FWM using polarization-resolved driving: $\mathcal{E}_3$ induces the FWM signal in a given valley, which originates from the population generated in the counter- or co-polarized valley, by setting counter- or co-circular $\mathcal{E}_{1,2}$, respectively. Top: τ_{23} delay dependence of the measured circular polarization degree, $\rho(\tau_{23})$. We measure $\rho(\tau_{23})$ of several tens of % for initial delays τ_{23}, followed by a total depolarization of the FWM, generated by the secondary (see the main text) exciton population.

top of Fig. 5. We thus do observe a significant pseudo-spin polarisation around zero delay, $\rho(\tau_{23}) \simeq 0) \simeq 30\%$, which however vanishes extremely rapidly, within around 5 ps, such that $\rho(\tau_{23}) = 0$ for $\tau_{23} > 10$ ps. We therefore show that under resonant excitation it is possible to generate valley-polarized excitons in $MoSe_2$ monolayers, but confirm their rapid depolarization. This result brings new input towards a firm understanding of an intriguingly

weak efficiency of optical pumping in $MoSe_2$ monolayers, as opposed to other S-TMDs.[45] The circular polarization degree, relevant for valleytronics applications, could be stabilized by using magnetic fields [38] or by fabricating more involved hetero-structures [46,47] based on S-TMDs.

When analyzing Fig. 5 it is worth to note a large fraction of the FWM response within initial several ps for both polarization configurations, as compared to the subsequent dynamics. This shows that the exciton density is mainly removed radiatively within the sub-ps radiative lifetime T_1, as discussed before.

Conclusions By performing FWM spectroscopy, we have demonstrated a giant, optical, coherent, nonlinear response of exciton transitions in $MoSe_2$ monolayers. We find an increase in the FWM amplitude by two orders of magnitude, as compared to a high quality CdTe semiconductor quantum well (not shown), emitting at the similar wavelength and excitation power. Taking advantage of the microscopy approach, we have performed the hyperspectral imaging, which allowed us to accurately determine the areas yielding FWM responses of either neutral, or charged excitons, or both. Electrical gating of such structures could enable spectral control of coherent responses from TMDs, providing insights into the mutual influence of TR and EX onto their dynamics. Using two-beam FWM micro-spectroscopy, we have measured the excitons' coherence evolution, accessing dephasing times T_2, which turn out to be intrinsically limited by the radiative lifetime. The inhomogeneous broadening on a sub-μm range is reduced by an order of magnitude with respect to the size of the flake, although still gives rise to the photon echo. We have also shown that T_2 spatially varies across the flake, as the T_1 is governed by the local disorder, determining the exciton localization. Microscopic measurement of the FWM response is therefore required to accurately assess these parameters. Prospective experiments, exploiting two-dimensional FWM spectroscopy, will ascertain coupling mechanisms between exotic valley-exciton species offered by S-TMDs. Our approach could be used to retrieve coherent responses of the localized

exciton states in S-TMDs,[48] which are expected to exhibit ultra-long dephasing.[49] Finally, by exploiting polarization-resolved, three-beam FWM we assessed the exciton population dynamics, revealing the interplay between the sub-ps radiative decay T_1 and the intra-valley relaxation T_{intra} of the excitons scattered towards the dark states, revisiting the light-matter coupling in two-dimensional systems.[5]

We acknowledge the support by the ERC Starting Grant PICSEN contract no. 306387 and the ERC Advanced Grant MOMB contract no. 320590. We thank G. Nogues and M. Richard for helpful remarks on the manuscript. We also acknowledge the support from Nanofab facility of the Institute Néel, CNRS UGA.

References

(1) Novoselov, K. S.; Geim, A. K.; Morozov, S. V.; Jiang, D.; Zhang, Y.; Dubonos, S. V.; Grigorieva, I. V.; Firsov, A. A. *Science* **2004**, *306*, 666–669.

(2) Fiori, G.; Bonaccorso, F.; Iannaccone, G.; T.Palacios,; Neumaier, D.; Seabaugh, A.; Banerjee, S. K.; Colombo, L. *Nat. Nanotech.* **2014**, *10*, 768–779.

(3) Koppens, F. H. L.; Mueller, T.; Avouris, P.; Ferrari, A. C.; Vitiello, M. S.; Polini, M. *Nat. Nanotech.* **2014**, *10*, 780–793.

(4) Mak, K. F.; Lee, C.; Hone, J.; Shan, J.; Heinz, T. F. *Phys. Rev. Lett.* **2010**, *105*, 136805.

(5) Deveaud, B.; Clérot, F.; Roy, N.; Satzke, K.; Sermage, B.; Katzer, D. S. *Phys. Rev. Lett.* **1991**, *67*, 2355.

(6) Ye, Z.; Cao, T.; O'Brien, K.; Zhu, H.; Yin, X.; Wang, Y.; Louie, S.G.; Zhang, X.; *Nature* **2014**, *513*, 214–218.

(7) Chernikov, A.; Berkelbach, T.C.; Hill, H.M.; Rigosi, A.; Li, Y.; Aslan, O.B.; Reichman, D.R.; Hybertsen, M.S.; Heinz, T.F. *Phys. Rev. Lett.* **2014**, *113*, 076802.

(8) Wang, G.; Marie, X.; Gerber, I.; Amand, T.; Lagarde, D.; Bouet, L.; Vidal, M.; Balocchi, A.; Urbaszek, B. *Phys. Rev. Lett.* **2015**, *114*, 097403.

(9) Olsen, T.; Latini, S.; Rasmussen, F.; Thygesen, K. S. *Phys. Rev. Lett.* **2016**, *116*, 056401.

(10) Leavitt, R. P.; Little, J. W. *Phys. Rev. B* **1990**, *42*, 11774.

(11) Andreani, L. C. In *Confined Electrons and Photons: New Physics and Applications*; Burstein, E., Weisbuch, C., Eds.; Nato Science Series: B Physics; Plenum Press: New York, 1995; Vol. 340; pp 57–112.

(12) Arora, A.; Koperski, M.; Nogajewski, K.; Marcus, J.; Faugeras, C.; Potemski, M. *Nanoscale* **2015**, *7*, 10421–10429.

(13) Palummo, M.; Bernardi, M.; Grossman, J. C. *Nano Lett.* **2015**, *15*, 2794.

(14) Poellmann, C.; Steinleitner, P.; Leierseder, U.; Nagler, P.; Plechinger, G.; Porer, M.; Bratschitsch, R.; Schüller, C.; Korn, T.; Huber, R. *Nat. Mater.* **2015**, *14*, 889–893.

(15) Moody, G.; Dass, C. K.; Hao, K.; Chen, C.-H.; Li, L.-J.; Singh, A.; Tran, K.; Clark, G.; Xu, X.; Berghaüser, G.; Malic, E.; Knorr, A.; Li, X. *Nat. Comm.* **2015**, *6*, 8315.

(16) Liu, X.; Galfsky, T.; Sun, Z.; Xia, F.; chen Lin, E.; Lee, Y.-H.; Kéna-Cohen, S.; Menon, V. M. *Nat. Phot.* **2014**, *9*, 30–34.

(17) Malard, L. M.; Alencar, T. V.; Barboza, A. P. M.; Mak, K. F.; de Paula, A. M. *Phys. Rev. B* **2013**, *87*, 201401(R).

(18) Lagarde, D.; Bouet, L.; Marie, X.; Zhu, C. R.; Liu, B. L.; Amand, T.; Tan, P. H.; Urbaszek, B. *Phys. Rev. Lett.* **2014**, *112*, 047401.

(19) Hao, K.; Moody, G.; Wu, F.; Dass, C. K.; Xu, L.; Chen, C.-H.; Li, M.-Y.; Li, L.-J.; MacDonald, A. H.; Li, X. *Nat. Phys.* **2016**, *12*, 667.

(20) Fras, F.; Mermillod, Q.; Nogues, G.; Hoarau, C.; Schneider, C.; Kamp, M.; Höfing, S.; Langbein, W.; Kasprzak, J. *Nat. Phot.* **2016**, *10*, 155.

(21) Langbein, W.; Patton, B. *Phys. Rev. Lett.* **2005**, *95*, 017403.

(22) Wang, G.; Palleau, E.; Amand, T.; Tongay, S.; Marie, X.; Urbaszek, B. *Appl. Phys. Lett.* **2015**, *106*, 112101.

(23) Jones, A. M.; Yu, H.; Ghimire, N. J.; Wu, S.; Aivazian, G.; Ross, J. S.; Zhao, B.; Yan, J.; Mandrus, D. G.; Xiao, D.; Yao, W.; ; Xu, X. *Nat. Nanotech.* **2016**, *8*, 634.

(24) Langbein, W.; Runge, E.; Savona, V.; Zimmermann, R. *Phys. Rev. Lett.* **2002**, *89*, 157401.

(25) Kasprzak, J.; Patton, B.; Savona, V.; Langbein, W. *Nat. Phot.* **2011**, *5*, 123.

(26) Langbein, W. *Rivista del nuovo cimento* **2010**, *33*, 255–312.

(27) Naeem, A.; Masia, F.; Christodoulou, S.; Moreels, I.; Borri, P.; Langbein, W. *Phys. Rev. B* **2015**, *91*, 121302(R).

(28) Singh, A.; Moody, G.; Wu, S.; Wu, Y.; Ghimire, N. J.; Yan, J.; Mandrus, D. G.; Xu, X.; Li, X. *Phys. Rev. Lett.* **2014**, *112*, 216804.

(29) Hao, K.; Xu, L.; Nagler, Ph.; Singh, A.; Tran, K.; Dass, Ch.; Schuller, Ch.; Korn, T.; Li, X.; Moody, G. *Nano Letters* **2016**, *16*, 5109.

(30) Masia, F.; Langbein, W.; Moreels, I.; Hens, Z.; and Borri, P. *Phys. Rev. B* **2011**, *83*, 201305(R).

(31) An, J. M.; Franceschetti, A.; and Zunger, A. *Nano. Lett.* **2007**, *7*, 2129.

(32) Qiu, D. Y.; Cao, T.; Louie, S. G. *Phys. Rev. Lett.* **2015**, *115*, 176801.

(33) Xiao, D.; Liu, G.-B.; Feng, W.; Xu, X.; Yao, W. *Phys. Rev. Lett.* **2012**, *108*, 196802.

(34) Jones, A. M.; Yu, H.; Ghimire, N. J.; SanfengWu,; Aivazian, G.; Ross, J. S.; Zhao, B.; Yan, J.; Mandrus, D. G.; Xiao, D.; Yao, W.; Xu, X. *Nat. Nanotech.* **2013**, *8*, 634–638.

(35) Xu, X.; Yao, W.; Xiao, D.; Heinz, T. F. *Nat. Phys.* **2014**, *10*, 343–350.

(36) Yu, T.; Wu, M. W. *Phys. Rev. B* **2014**, *89*, 205303.

(37) Glazov, M. M.; Amand, T.; Marie, X.; Lagarde, D.; Bouet, L.; Urbaszek, B. *Phys. Rev. B* **2014**, *89*, 201302(R).

(38) Smoleński, T.; Goryca, M.; Koperski, M.; Faugeras, C.; Kazimierczuk, T.; Nogajewski, K.; Kossacki, P.; Potemski, M. *Phys. Rev. X* **2016**, *6*, 021024.

(39) Zhang, X.-X.; You, Y.; Zhao, S. Y. F.; Heinz, T. F. *Phys. Rev. Lett.* **2015**, *115*, 257403.

(42) Wang, G.; Robert, C.; Suslu, A.; Chen, B.; Yang, S.; Alamdari, S.; Gerber, I. C.; Amand, T.; Marie, X.; Tongay, S.; Urbaszek, B. *Nat. Comm.* **2015**, *6*, 10110.

(41) Horzum, S.; Sahin, H.; Cahangirov, S.; Cudazzo, P.; Rubio, A.; Serin, T.; Peeters. F.M.; *Phys. Rev. B.* **2013**, *87*, 125415.

(42) Wang, G.; Robert, C.; Suslu, A.; Chen, B.; Yang, S.; Alamdari, S.; Gerber, I. C.; Amand, T.; Marie, X.; Tongay, S.; Urbaszek, B. *Nat. Comm.* **2015**, *6*, 10110.

(43) Echeverry, J. P.; Urbaszek, B.; Amand, T.; Marie, X.; Gerber, I. C. *Phys. Rev. B* **2016**, *93*, 121107.

(44) Withers, F. et al. *Nano Lett.* **2015**, *15*, 8223–8228.

(45) Dery, H.; and Song, Y. *Phys. Rev. B* **2015**, *92*, 125431.

(46) Rivera, P.; Schaibley, J. R.; Jones, A. M.; Ross, J. S.; Wu, S.; Aivazian, G.; Klement, P.; Seyler, K.; Clark, G.; Ghimire, N. J.; Yan, J.; Mandrus, D. G.; Yao, W.; Xu, X. *Nat. Comm.* **2015**, *6*, 6242.

(47) Rivera, P.; Seyler, K. L.; Yu, H.; Schaibley, J. R.; Yan, J.; Mandrus, D. G.; Yao, W.; Xu, X. *arXiv:1601.02641* **2016**.

(48) Koperski, M.; Nogajewski, K.; Arora, A.; Cherkez, V.; Mallet, P.; Veuillen, J.-Y.; Marcus, J.; Kossacki, P.; Potemski, M. *Nat. Nanotech.* **2015**, *10*, 503–506.

(49) Schaibley, J. R.; Karin, T.; Yu, H.; Ross, J. S.; Rivera, P.; Jones, A. M.; Scott, M. E.; Yan, J.; Mandrus, D. G.; Yao, W.; Fu, K.-M.; Xu, X. *Phys. Rev. Lett.* **2015**, *114*.